Journal of Structural Biology 171 (2010) 361–371

Contents lists available at ScienceDirect

Journal of Structural Biology

journal homepage: www.elsevier.com/locate/yjsbi

# X-ray μCT imaging technique reveals corm microstructures of an arctic-boreal cotton-sedge, *Eriophorum vaginatum*

Sarah J. Bogart [a], Graeme Spiers [a], Ewa Cholewa [b,*]

[a] Centre for Environmental Monitoring and Department of Biology, Laurentian University, 935 Ramsey Lake Road, Sudbury, Ont., Canada P3E 2C6
[b] Department of Biology, Nipissing University, 100 College Drive, North Bay, Ont., Canada P1B 8L7

ARTICLE INFO

*Article history:*
Received 20 March 2010
Received in revised form 4 June 2010
Accepted 4 June 2010
Available online 10 June 2010

*Keywords:*
X-ray μCT
Microtomography
*Eriophorum vaginatum*
Cotton-sedge
Sclereid clusters
3D image

ABSTRACT

X-ray computed tomography (CT), a non-destructive imaging technique, has recently been effectively applied to botanical research. In this study an X-ray μCT technique was developed to allow for anatomical study of the overwintering corms of *Eriophorum vaginatum*, an ecologically important sedge species in arctic tussock-tundra and boreal peatlands. Using a GE Medical MS8X-130 X-ray μCT scanner, optimal imaging parameters included scanning isolated corms at 80 kVp and 100 μA with a 3500 ms exposure time and an isotropic voxel size of 10 μm. A Gaussian blur image filter with a blur radius ($\sigma$) of two pixels was applied to the optimal dataset to improve visual detection and contrast of tissues while removing 99.2% of image noise. Using the developed X-ray μCT technique several undocumented anatomical characteristics of the corm were identified including the vascular connection between a parent corm and branching cormel and the 3D shape of sclereid clusters. The 3D structure of sclereid clusters was determined whereby the perimeter of their lance shape is greatly reinforced by sclereids with thicker secondary cell walls as compared to those of the interior of the cluster. The structure of sclereid clusters and their association with leaf traces suggests they may be stabilizing the corm-leaf connection to protect vascular tissues from physical damage. The proposed X-ray μCT technique is an excellent tool for determination of the 3D structure of *E. vaginatum* corms and may be used to detect alterations in tissue structure and chemistry in response to environmental change in this and other Cyperaceous species.



## 1. Introduction

X-ray computed tomography (CT) is a non-destructive imaging technique that utilizes the variability in the density and chemical composition of samples to form images (Hounsfield, 1973). Originally designed as a medical diagnostic tool, X-ray CT scanners form images by exposing a sample to a polychromatic X-ray beam. X-rays are differentially absorbed by the sample which produces a 2-dimensional (2D) "view", with many views produced at many angles to the sample and being combined mathematically into a 3D image. This 3D image represents the radiodensity of the sample and can provide a structural map of its internal components. X-ray CT has proved useful in quantifying the internal structure of samples from a variety of disciplines including biology (Stock et al., 2003), histology (Cnudde et al., 2008), palaeontology (Sutton, 2008), geology (Ketcham and Carlson, 2001), thermochronology (Evans et al., 2008), hydrology (Wildenschild et al., 2002), soil science (Elliot and Heck, 2007a, 2007b; Jassogne et al., 2007; Torrance et al., 2008), and materials science (Wang, 2007; Tondi et al., 2009).

The use of X-ray computed tomography (CT) for botanical research is of interest due to the potential advantages of this imaging method over classical means of sectioning and microscopy. Sample processing prior to image acquisition, such as dehydration, embedding, or sectioning is not required meaning digital sections can be obtained in less time and without structural alterations, such as tissue compression or tearing, that are prevalent in physically sectioned samples (Steppe et al., 2004). As X-ray CT imaging is non-destructive, repeated scanning or additional sampling techniques can be applied to the same sample (Dutilleul et al., 2005). Imagery from X-ray CT scans can also be viewed and re-viewed at virtually any sectioned slice angle in 2D or 3D. Alternatively objects of interest can be segmented from the images as digital surfaces, or isosurfaces, making it easier to analyse complex structures or samples difficult to section using classical techniques (Evans et al., 2008). Resolutions near the micron level can be achieved for cm-sized samples using X-ray μCT (Cnudde et al., 2008; Evans et al., 2008) while <1 μm resolution can be achieved for mm-sized samples using X-ray sub-micronCT (Van den Bulcke et al., 2009a). Recent botanical applications of X-ray CT techniques have included obtaining taxonomically significant anatomy of pyritized fossil fruit (DeVore et al., 2006), determination of wood anatomy (Steppe et al., 2004) and wood water content (Fromm et al., 2001),

* Corresponding author. Fax: +1 705 474 1947.
*E-mail addresses:* sbogart@mirarco.org (S.J. Bogart), gspiers@mirarco.org (G. Spiers), ewac@nipissingu.ca (E. Cholewa).

1047-8477/$ - see front matter © 2010 Elsevier Inc. All rights reserved.
doi:10.1016/j.jsb.2010.06.009

assessing fungal decay of wood (Van den Bulcke et al., 2009b), quantification of canopy growth of tree seedlings (Dutilleul et al., 2005, 2008), characterization of plant roots in soil (Pierret et al., 2005; Lontoc-Roy et al., 2006; Hamza et al., 2007), and quantification of the spatial distribution of leaf trichomes on *Arabidopsis thaliana* (Kaminuma et al., 2008).

*Eriophorum vaginatum*, a "cotton-sedge", is ecologically significant to boreal peatlands and arctic tussock-tundra where it is often the dominant, herbaceous vascular species (Polozova, 1970; Wein, 1973; Chapin et al., 1979, 1993; Lavoie et al., 2003), being forage for muskoxen, caribou, deer, and sheep (Wein, 1973; Duffy et al., 2001). *E. vaginatum* readily colonizes disturbed sites and thrives in open areas with nutrient poor substrates comprised of peat or wet, fine-grained soils, often overlaying permafrost (Polozova, 1970; Chapin et al., 1979; Lavoie et al., 2003). The elevated tussock growth form of *E. vaginatum* creates its own microenvironment (Chapin et al., 1979), which is thought to provide varied microsites for the establishment of other successive species (Polozova, 1970; Lavoie et al., 2003). *E. vaginatum* can survive tundra fires (Wein, 1973; Racine et al., 1987), extensive, repeated, simulated herbivory (Archer and Tieszen, 1983), and periodic drought (Wein, 1973). *E. vaginatum* can grow in soils with a wide range in pH, from ~3 to 8 (Wein, 1973; Stevens, 2006) and has been grown successfully on peat amended kimberlite, a waste product from diamond mining (Stevens, 2006). Moreover, this species can endure anthropogenic stressors such as $^{137}$Cs fallout from the Chernobyl accident (Jones et al., 1998), crude oil spills on tundra (Racine, 1994), and in peatlands that have been aerially polluted by Pb, Fe, and Cu–Ni smelting (Markert and Thornton, 1990; Huopalainen et al., 2000). Hence, *E. vaginatum* is of interest on an ecological basis, as a potential species for revegetation of vacuum-mined peatlands, and for pollutant biostabilization in industrially damaged wetlands.

Evidently *E. vaginatum* existence and persistence in adverse environments depends on the vitality of its overwintering corms (Chapin et al., 1979; Archer and Tieszen, 1983; Racine et al., 1987; Racine, 1994). To elucidate the survival mechanisms of corms, a detailed understanding of corm anatomy and tissue relationships is required. We present a method to non-destructively image the corm tissues of *E. vaginatum* using X-ray μCT. The specific objectives were (i) to develop an X-ray μCT technique to non-destructively image live, hydrated corms of *E. vaginatum* and (ii) to apply this technique to reveal tissue architecture of the corm. This study investigates tissue structure relationships within the corm of *E. vaginatum* with implications on species survival.

## 2. Materials and methods

### 2.1. Plant material

Tussocks of *E. vaginatum* were collected during the summer of 2007 from a wetland near Cartier, Ontario, Canada (46°39′42″N, 81°31′14″W). The site was an open, black-spruce dominated peatland with *Picea mariana* (Mill.) B.S.P., *Ledum* sp., *Chamaedaphne calyculata* (L.) Moench., *E. vaginatum*, *E. virginicum* L., *Kalmia angustifolia* L., *K. polifolia* Wangenh., *Vaccinium oxycoccus* L., *Sphagnum* spp., and *Carex oligosperma* Michx. being the predominant species present. *E. vaginatum* tussocks were approximately 30 cm in diameter and 50 cm tall (from peat surface to top of leaves). The tussocks were complex networks of tillers comprised of tightly branching corms, adventitious roots, leaves, and vertical rhizomes.

### 2.2. Light microscopy

To identify corm tissues and their structural relationships using conventional light microscopy, living corms from collected tussocks were hand-sectioned with razor blades and observed with an Olympus CX-41 light microscope equipped with an Olympus Q-Colour 3 digital camera (Olympus America Inc., USA) for image capture, with images being adjusted for brightness and contrast as required using Adobe Photoshop CS3 Extended v10.0.1 (Adobe Systems Incorporated, USA).

### 2.3. X-ray μCT scanning

Sample preparation was not required for X-ray μCT scanning other than to size them appropriately to fit into the scanning tubes. For low resolution scans, a tussock was representatively sub-sampled and leaves were trimmed to 0.5 cm above corms. Any peat and loose decaying material was removed using tap water to simplify image interpretation after scanning. For high resolution scans of corms, individual tillers were removed from the tussock and living corms were isolated from all other material to maximize the number of corms scanned, however, corm branching architecture was preserved. Samples were stabilized within the scanning tubes where required by using radiolucent foam pieces placed outside of the scanned region.

Plant material was scanned using a GE Medical (formerly Enhanced Vision Systems, London, Ontario, Canada) MS8X-130 X-ray μCT system which uses a tungsten target, microfocus X-ray tube as the X-ray source. The detector in this X-ray μCT scanner has been rotated 90° to allow samples of wider dimensions to be scanned (Elliot, personal communication). Corms were scanned at 80 kVp, 100 μA using two high-pass filters (Cu) to reduce beam hardening effects on images, which appear in X-ray CT images as a brightened edge near the exterior of the scanned region and a darkened centre (Ketcham and Carlson, 2001). Beam filtration using a high-pass filter reduces beam hardening artefacts by pre-hardening the X-ray beam, which reduces the number of low energy photons interacting with the object (Kalender, 2005). Three isotropic voxel resolutions of 50, 20, and 10 μm (Table 1) were used to determine their effect on corm tissue differentiation and image noise. Attempts to maximize soft tissue contrast at lower kVp and at 6 μm voxel resolution, near the limit of this system, resulted in images of poorer quality than the optimal dataset of 10 μm voxel resolution, even after image filtering (data not shown). Each scan combined 720 views of the plant material over 360° sample rotation and was reconstructed into signed, 16-bit image volumes using GE Medical proprietary software. X-ray absorbance of image volumes was calibrated to Hounsfield Units (HU) using air and water standards contained in microcentrifuge-tubes and scanned with the corm samples. Representative corm volumes incorporating several corm internodes, i.e. between 132 and 382 axial image slices, were cropped from the original image volumes using the ROI tool within GE-HC SliceView v.1.1. (http://sourceforge.net/project/showfiles.php?group_id=69063). For comparison with hand-sections of live plant material, image orientation is referred to such that the axial *Z* image plane is synonymous with cross-sections of corms while the *X* and *Y* orthogonal planes (coronal and sagittal) are synonymous with longitudinal sections, as the corm can be considered radially symmetrical.

**Table 1**
Parameters for X-ray μCT scans of *E. vaginatum* corms at 80 kVp, 100 μA.

| Voxel resolution ($\mu m^3$) | Sample tube diameter (mm) | Exposure time (ms) | Distance from source (mm) | Detector binning |
|---|---|---|---|---|
| 50 | 64 | 1700 | 300 | 2 × 2 |
| 20 | 28 | 1700 | 120 | 2 × 2 |
| 10 | 12 | 3500 | 120 | 1 × 1 |

### 2.4. Image processing

To determine the amount of a Gaussian blur to apply to images, a blur series was created using a representative image from the 10 μm dataset. Image noise profiles, denoting pixel HU values over a specified distance, were created across a common line of 1000 voxels for each image of the blur series were created to visually compare the effect of increasing the amount of the image blur on image noise. The percent difference in image noise of the blur series was computed to determine the statistical effect of increasing the amount of image blur on image noise. Image noise was calculated as the standard deviation of all voxel values (in HU) of each image in the blur series. Image histograms were calculated for each 2D axial image and their respective image volumes to determine blur effect on histogram shape.

Application of the Gaussian blur filter was using the program GE-HC MicroView v.2.1.2 (http://sourceforge.net/projects/microview/). A corm image volume was imported into MicroView and one copy was immediately exported as a sequential series of signed, 16-bit axial slices in DICOM format. Copies of the original volume were further processed by application of various levels of the Gaussian blur filter using the built-in Gaussian smoothing function of MicroView. The blurred image volumes were also exported as DICOM formatted axial image slices such that a slice within a corm could be compared between original and blurred images.

Representative axial slices exported from image volumes were imported into ImageJ v.1.41b (http://rsbweb.nih.gov/ij/index.html) to calculate image histograms of the axial images and their volumes. To allow computation of image histograms for the respective corm volumes, the Import DICOM Sequence plugin of ImageJ was used to load multiple slices as a volume. Histogram data was exported from ImageJ as text data and constructed into standard graphs using Microsoft Excel v.10.26 (Microsoft Corporation, USA).

The corm image volume considered optimal after blurring was used to create a preliminary 3D tissue maps, or isosurfaces, of sclereid clusters for comparison to tissue structure patterns identified in light micrographs. The histogram thresholding function built into MicroView was used to identify thresholds based on the image histogram of tissue volumes incorporating between 15,000 and 20,000 voxels, which were manually chosen to encompass only the tissue of interest and its background, an immediately adjacent tissue. This maximized peak resolution in the image histograms and improved segmentation results. Isosurfaces, or digital tissue maps, were generated and visually compared to tissue patterns identified using light microscopy. Removal of extraneous data from isosurfaces, i.e. fragments produced from secondary corms within the primary corm volumes, was performed manually within ParaView 3.2.1 (www.paraview.org).

## 3. Results and discussion

### 3.1. Corm localization and macroscopic features

The tussock of *E. vaginatum* is a dense, complex mass of tillers comprised of corms, vertical rhizomes, leaves, leaf bases, and roots. Within tillers (Fig. 1A), corms (Fig. 1A, box) were sheathed by leaf bases and spatially separated by vertical rhizomes (Fig. 1A, arrows). Corms were easily differentiated from vertical rhizomes as corms are thicker in diameter and exhibit shorter internodes than vertical rhizomes. Moreover, all adventitious roots originate from corms. Polozova (1970) also determined that the tillers of *E. vaginatum* are comprised of two different shoot types, one being rhizomatous the other not. Longitudinal dissection of the corms exposed sclereid clusters aligned parallel to the longitudinal axis of the corm (Fig. 1B, arrowheads). These sclereid clusters may facilitate nutrient translocation within the corm (Cholewa and Griffith, 2004) and require further investigation as to their functional role within *E. vaginatum*.

### 3.2. Anatomy of the corm: Optical knowledge can be acquired digitally

The internal anatomy the corm was revealed in hand-sections of fresh corms, observed by light microscopy (Fig. 1C). A single layer of epidermal cells (Fig. 1C, e) surrounded a multi-layered exodermis (Fig. 1C, ex), which sporadically included groups of fibres (Fig. 1C, f). Centripetal to these protective outer layers was a cortex (Fig. 1C, co) consisting of a matrix of parenchyma and aerenchyma (Fig. 1C, a). Parenchymatous ground tissue (Fig. 1C, p) was also apparent within the vascular cylinder encircled by a horizontal vascular ring (Fig. 1C, vr). Vascular bundles and red–orange sclereid clusters were predominately located within this vascular cylinder (Fig. 1C, vb and scl). These results confirm general earlier observations by Metcalfe (1971) and a detailed description of the corm by Cholewa and Griffith (2004).

While the anatomy of the corm can be observed in 2D using conventional light microscopy, these structures of the corm can also be successfully visualized using X-rays with X-ray μCT (Fig. 1D). Albeit X-ray μCT has the additional advantage that tissues can be viewed in several planes, such as axial, sagittal, and coronal planes (Fig. 1D, right top to bottom, respectively) without requiring sample destruction. X-ray μCT image planes can also be viewed simultaneously as a planar image cube (Fig. 1D, left), meaning complex structures can be observed in 3D without sectioning many samples at different angles, an excellent advantage of X-ray μCT over traditional light microscopy.

### 3.3. Effect of X-ray μCT voxel resolution on corm tissue differentiation

Fig. 2 demonstrates the differentiation of corm tissues in a voxel resolution-series acquired with X-ray μCT using a standard X-ray tube potential (80 kVp) and current (100 μA). Generally, as voxel resolution was improved by reducing isotropic voxel dimensions from 50 to 20 to 10 μm, tissues of the corm became increasingly recognizable (Fig. 2A–C, respectively).

At 50 μm voxel resolution, corm images did not contain sufficient information to be useful in tissue analysis as only basic features of the corm could be visualized (Fig. 2A, A1). The outer protective layers, cortex, and vascular cylinder could be identified but all features had extremely vague boundaries (Fig. 2A, d, co, and vc). However, the interface between parent corms and their outgrowing cormels, or the corm-cormel interface, can be recognized (Fig. 2A, arrow). The images at this resolution may be useful in determining the branching architecture of *E. vaginatum* tillers.

The 20 μm voxel resolution images (Fig. 2B) revealed most corm tissues observed in light micrographs (Fig. 1A) and the voxel boundaries of tissues were not as vague as those of the 50 μm voxel resolution dataset. Limitations of the 20 μm dataset included a visual combination of several tissues including the epidermis, exodermis, and related fibres being represented as a single region, which also incorporated adjacent, wet, dead organic material, such as senesced leaf bases (Fig. 2B, ∗), when these were present. The differentiation of aerenchyma and parenchyma within the cortex was incomplete, as only the largest intercellular spaces could be identified and these features were extremely vague (Fig. 2B, arrow). Not all vascular bundles were distinguishable from other tissues in the vascular cylinder (Fig. 2B, arrowhead). The 20 μm resolution was excellent for identification of adventitious roots and their contents were clearly visible (Fig. 2B, r). This resolution has the potential to be used in multiple modality studies of root systems, as it allows detection of root structure, which could com-

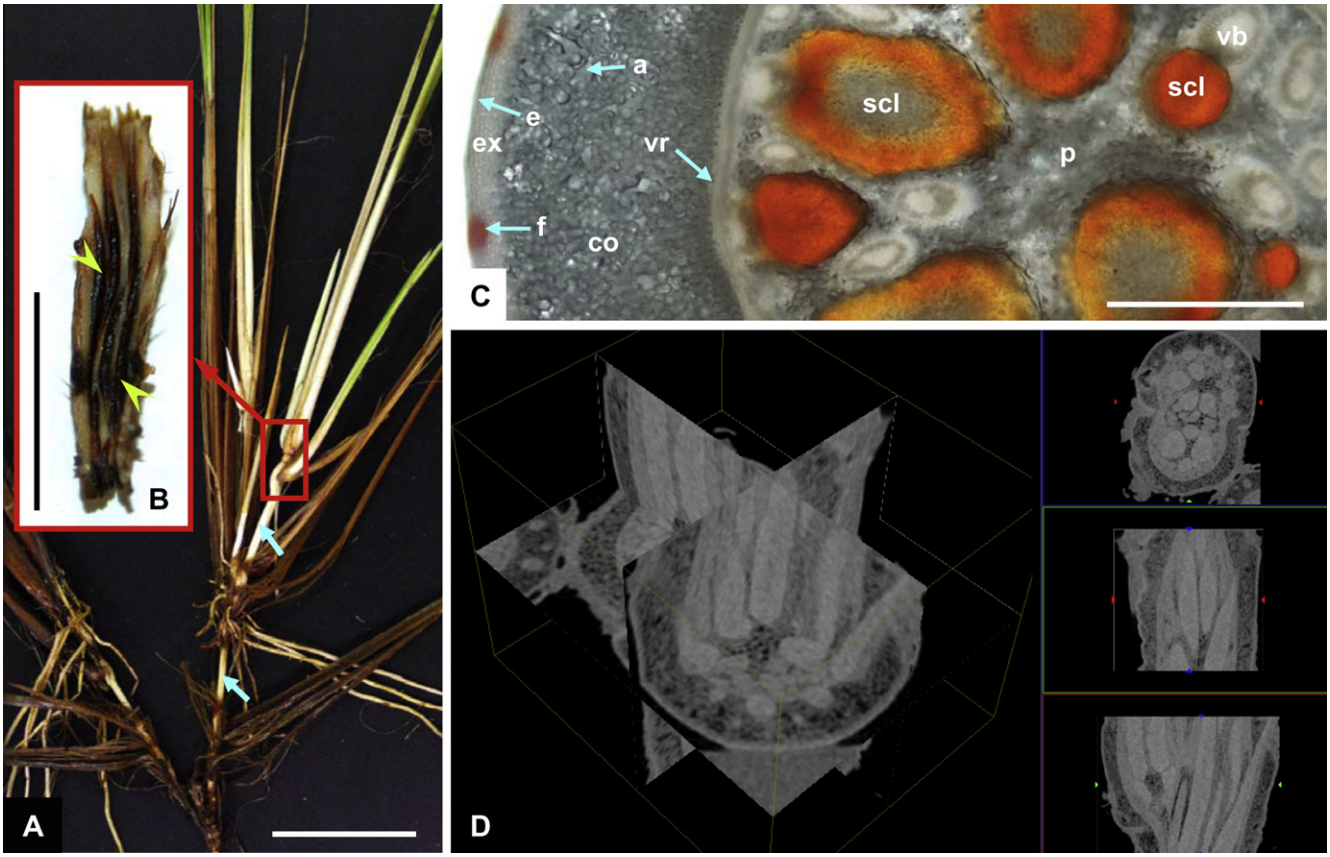


**Fig. 1.** (A–C) *E. vaginatum* corm localization and anatomy. (A) The tillers of individual tussocks are comprised of vertical rhizomes (arrows) and corms (box). Bar = 2.5 cm. (B) Longitudinal dissection of the corm exposed sclereid clusters (arrowheads) aligned parallel to the longitudinal axis of the corm. Bar = 1 cm. (C) Composite light micrograph of unstained cross-section of the corm of *E. vaginatum*. Anatomical features of the corm include an epidermis (e) and an exodermis (ex), which contains fibres (f). Centripetal to these tissues is the cortex (co) comprised of parenchyma (p) and aerenchyma (a). Vascular bundles (vb) and sclereid clusters (scl) are predominantly contained within a horizontal vascular ring (vr), comprising the vascular cylinder. Composite light micrograph was created by combining two light micrographs using the photomerge function within Photoshop CS3 Extended. Bar = 500 μm. (D) Corm of *E. vaginatum* visualized in multiple planes using X-ray μCT. Axial, coronal, and sagittal planes (right, top to bottom) can be viewed simultaneously in a planar cube (left). Note the similarity of tissues visualized in X-ray μCT as compared to light microscopy. Corm image cube is 4.0 × 5.1 × 3.8 mm. Images shown in insets are, from top to bottom, 4.0, 4.0, and 5.1 mm wide.

pliment current X-ray CT knowledge of root architecture and dynamics in soil (Pierret et al., 2005; Lontoc-Roy et al., 2006; Hamza et al., 2007; Jassogne et al., 2007).

The 10 μm voxel resolution images displayed a significant visual improvement in the delineation of tissue boundaries as compared to the 20 μm dataset (Fig. 2C). This improvement was especially noted in the delineation of aerenchyma and parenchyma in the cortex (Fig. 2C, arrow). In the corresponding image histogram, the peak near 0 HU, which represents the corm, exhibits a flattened apex ranging from about −400 to 200 HU (Fig. 2C1), meaning multiple peaks are present. As X-ray μCT is dependent on X-ray detectable variations in the density and chemical composition of samples to form images (Hounsfield, 1973), the successful imaging of plant tissues is largely based upon similarities in tissue composition including cell dimension, cell wall thickness, and contents (Stuppy et al., 2003). Thus, the multiple peaks within the corm peak represent individual tissues of the corm with overlapping radiodensities.

The image histograms of axial images (Fig. 2) are representative of their respective image histograms of the related image volumes (not shown). A flattened peak apex (Fig. 2C1), indicating the presence of multiple sub-peaks, was not observed in the 20 μm dataset (Fig. 2B1) making this image volume more difficult to interpret as there is more similarity in the radiodensity between tissues. Therefore, based on the clarity of anatomical details and the shape of the image histogram, the 10 μm resolution dataset was determined to be the optimal dataset and the most informative for analysis of the corm tissues.

However, the increase in voxel resolution to 10 μm also corresponded to an amplification of image noise. Small tissues with similar radiodensities became obscured and vascular bundles were less apparent as compared to those in the 20 μm image (Fig. 2B and C, vb). Increased mottling of the image was visually apparent in the images and in the highly variable X-ray attenuation values of the air peak at −1000 HU in the corresponding image histograms (Fig. 2B1 and C1). The increase in noise within the 10 μm dataset is likely quantum noise, which is inherent to the X-ray μCT technique and is due to the stochastic nature of X-ray attenuation processes (Farr and Allisy-Robers, 1998; Kalender, 2005). Hence, an image filter was required to reduce the effects of noise present in the optimal image volume and thereby improve tissue discernibility for accurate tissue identification.

### 3.4. Gaussian blur optimization

The Gaussian blur image filter approximates the profile of a Gaussian function along any row, column, or diagonal through the centre of the filter matrix (Russ, 1992). This filter is the basis of many mathematical algorithms commonly used as a processing step for signal and image analysis (Yang et al., 2003; Marziliano et al., 2004; Kawajiri et al., 2008) and, in this study, enhanced the visual contrast of tissues within corm images (Fig. 3). A Gauss-

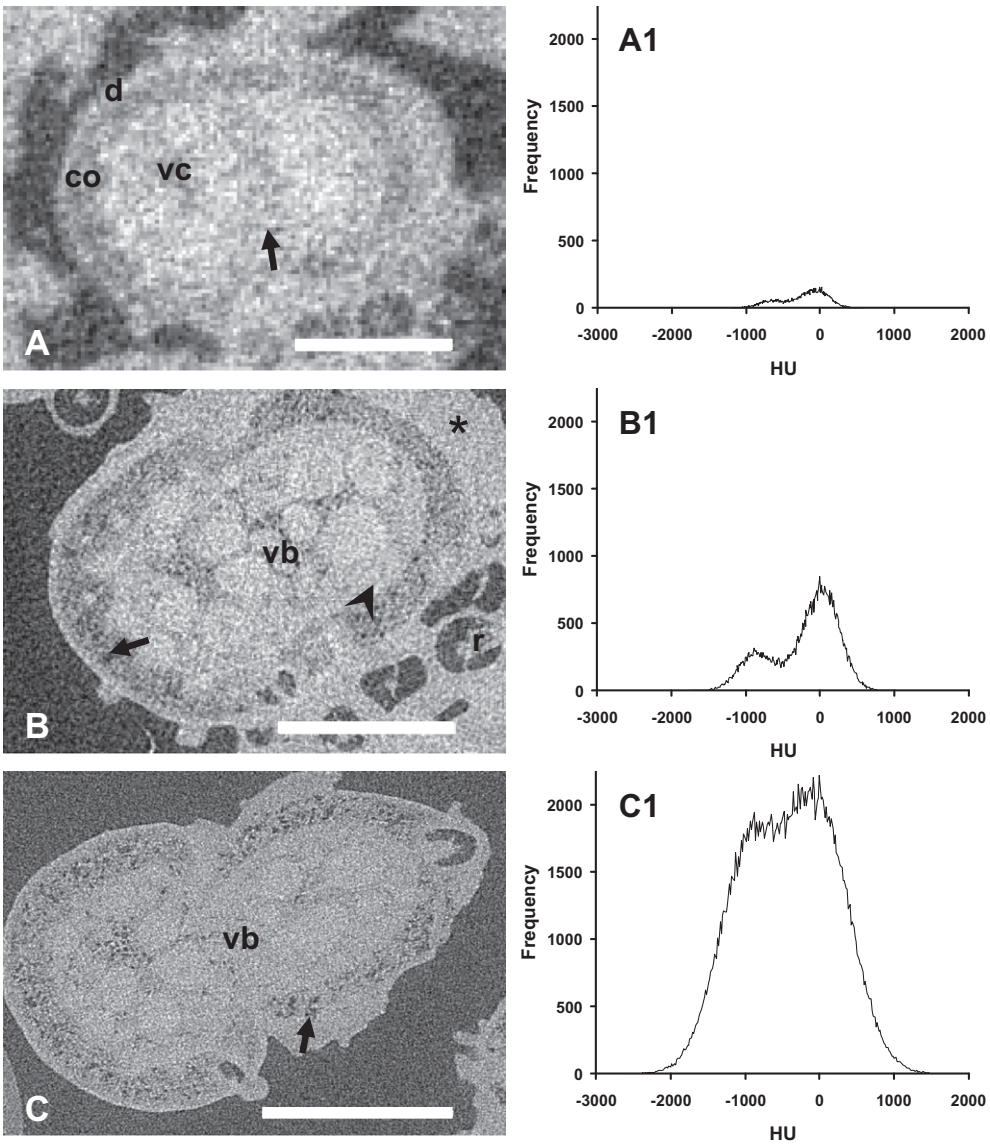


**Fig. 2.** (A–C) Voxel resolution-series of *E. vaginatum* corms scanned using X-ray μCT. Corms scanned at 50 μm (A), 20 μm (B), and 10 μm (C) isotropic voxel resolution using standard parameters of 80 kVp, 100 μA. (A1–C1) Corresponding axial image histograms of X-ray absorption expressed in Hounsfield Units (HU). Histograms are representative of the image volume. Arrow in (A) shows the interface between corm and cormel. In general, as voxel resolution was improved, image information increased whereby tissues became recognizable and tissue boundary delineation was refined. However, the amount of image noise was also amplified; note the large range in HU of the air peak in (C), air = −1000 HU. As a result small tissues which have similar radiodensity values are most obscured in (C). This is noted by the difficulty of identifying the vascular bundle (vb) in C as compared to in (B). Aerenchyma is well defined at 10 μm as compared to the 20 μm resolution image, arrows. Arrowhead in (B) delineates vascular tissues which are visually indistinct from other tissues of the vascular cylinder. Other features are as follows, d = epidermis and exodermis, co = cortex, vc = vascular ring, r = root, ∗ = wet, dead organic matter and adjacent epidermis and exodermis. Scale bars = 2 mm.

ian blur series was created using varying blur radii applied to X-ray μCT images of corms to determine the optimal blur radius for the 10 μm dataset (Fig. 3A–E). The amount of blur applied to images in the program MicroView is defined by blur radius whereby a larger radius results in more blur. In a Gaussian blur image filter the blur radius is the standard deviation ($\sigma$) of the function, measured in pixels (Russ, 1992). The blur radii ($\sigma$) used in the creation of the Gaussian blur image series (Fig. 3A–E) were 0, 1, 2, 3, and 4 pixels, respectively.

General trends of all images and related statistics in the blur series are that as the amount of blur increased, visual contrast and visual detection of tissues improved. Noise profiles and image histograms of axial images and their volumes were calculated for the corresponding Gaussian blur series (Fig. 3A1–E3) to determine the effect of noise reduction on images. As the variation in voxel HU values decreased (Fig. 3A1–E1), the corm and air peaks in the image histograms became differentiated. The image histograms calculated for the image volumes (Fig. 3A3–E3) are smoothed versions of those of the axial images (Fig. 3A2–E2), meaning axial images vary slightly but are generally similar throughout the corm. This relationship agrees with anatomical investigations of the corm whereby tissues vary slightly in their proportional distribution within cross-sections of the corm.

After image filtering, the corm peak in the image histogram was resolved as a multi-modal distribution (Fig. 3C2–E2) which was correlated with the presence of lignin and the thickness of secondary cell walls of cells comprising the tissues. In Fig. 3 (C2–E2), the peak near −300 HU primarily includes non-lignified tissues of the cortex while the peak near 0 HU is predominated by lignified tissues (vascular and sclerenchyma), however, there is an overlap in

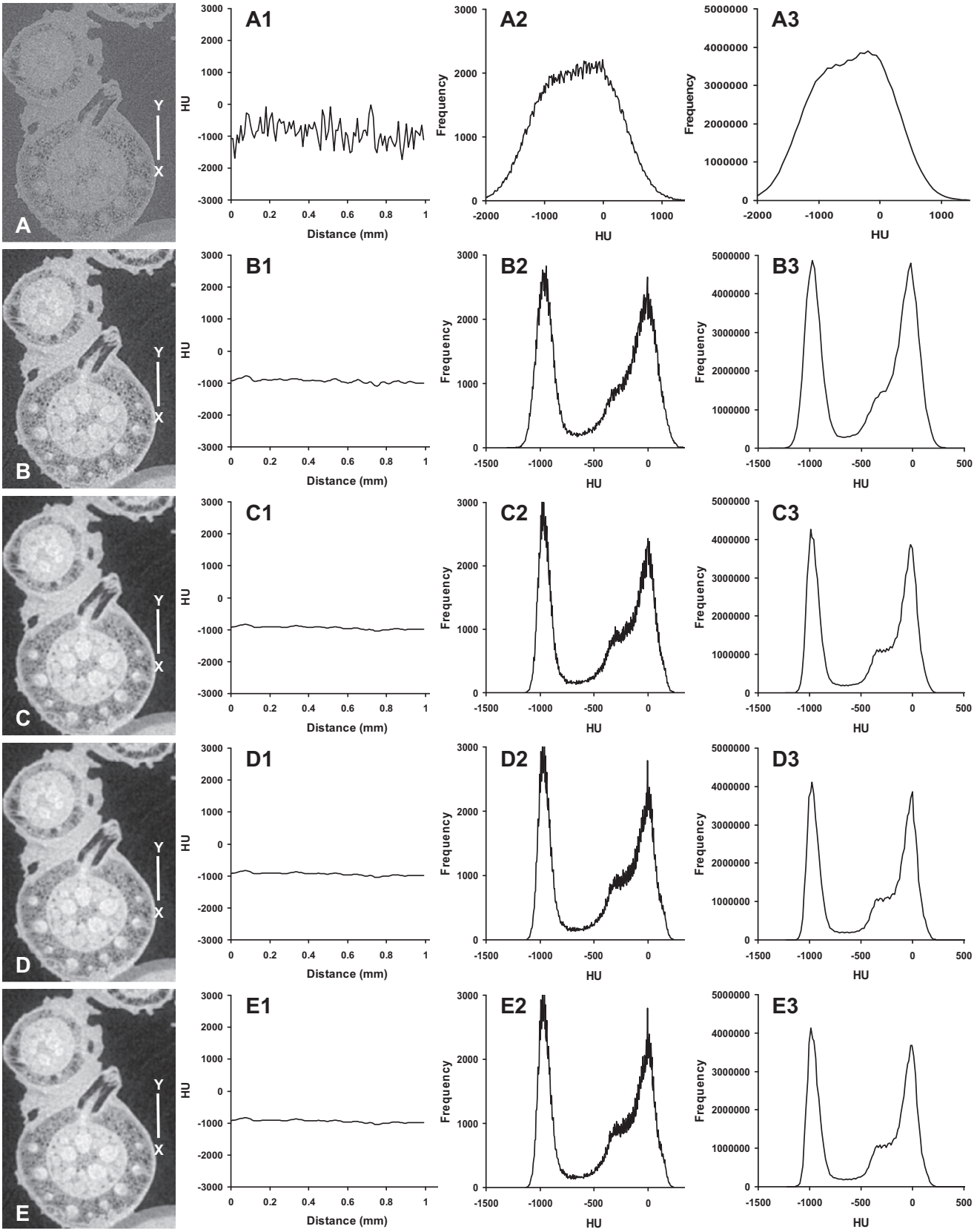


**Fig. 3.** (A–E) Effects of increasing the amount of a Gaussian blur image filter on an image series and related image statistics. The amount of blur applied to images increases from A to E whereby corresponding blur radii ($\sigma$) used in the production of images (A–E) are 0, 1, 2, 3, and 4 pixels, respectively, using the program MicroView (see text for details). Visual contrast and detection of tissues improves as blur amount increases. (A1–E1) Respective noise profiles of a standard line in air for images (A) to (E). Profile is from *x* to *y* of the line. Image noise, as the range of HU by which voxels vary, decreases as blur amount increases. (A2–E2) Respective image histograms for axial images shown in (A) to (E). Note flattened peak apex is present in unfiltered and filtered images. HU range is broader in (A2) and (A3) than in histograms of filtered images. HU scales of image histograms are standard only between filtered images to highlight peak differentiation as related to amount of blur applied. (A3–E3) Image histograms for the image volumes of axial images (A) to (E). Applying a Gaussian blur separated the air (−1000 HU) and corm (0 HU) peaks within the image histograms. Note there is little visual difference between images (C), (D), and (E) and their respective image statistics.

density between tissues. Lignin, often located within the secondary cell walls of plant cells, is a dense substance which is easily detected by X-ray CT, as demonstrated in wood research (Steppe et al., 2004; Van den Bulcke et al., 2009b). When comparing multiple *E. vaginatum* tissues by light microscopy using a classic histochemical technique (i.e. phloroglucinol–HCl, not shown), a range in the amount of lignin present within the secondary cell walls of cells comprising corm tissues is observable. Sclereid clusters, for example, have thick, extremely lignified, secondary cell walls in comparison to the sheath of cells surrounding vascular bundles, which is only partially lignified, and parenchyma, which has thin, non-lignified, primary cell walls. This difference in the amount of lignin present and secondary cell wall thickness can also be observed within a tissue, e.g. spatial variations in lignification and secondary cell wall thickness within sclereid clusters (discussed in Section 3.5). Our results agree with Stuppy et al. (2003), who noted that important factors in the differentiation of plant tissues in X-ray CT images are cell dimension, cell wall thickness, and contents, however, we add that these are confounding factors involved in differentiation of complex plant tissues by X-ray CT. Another factor important to X-ray CT differentiation of plant tissues is the packing structure of the primary and secondary cell wall components. While it is not currently possible to determine the structure of the primary and secondary cell walls of *E. vaginatum* corm tissues using our technique, knowledge gained from higher resolution imaging modalities, such as electron microscopy, may elucidate additional reasons for the overlap in radiodensity of corm tissues. Regardless, the presence of lignin in multiple tissues of *E. vaginatum* corms can be argued as a contributing factor to the similarity in radiodensity between tissues, and therefore, can be considered a type of plant-based noise in the X-ray μCT images.

Samples of this study consisted of living material, and therefore, water, being a major component of plant tissues, is likely also influencing the apparent similarity in the radiodensity of tissues. Leroux et al. (2009) found that critical point drying of samples improved tissue differentiation in X-ray nanoCT of *Asplenium theciferum* (Kunth) Mett. roots. Eliminating water caused the relative difference in radiodensities between tissues to be significantly increased, facilitating delineation by X-ray nanoCT. While critical point drying might have also improved differentiation, the present study demonstrates that the application of an appropriate image filter sufficiently enhanced X-ray μCT images for tissue-level study. Thereby, the extensive sample preparation of Leroux et al. (2009) was avoided and this allowed for the examination of living tissues. The examination of living tissues using X-ray CT is critical to the quantitative study of plant morphological response to the environment as each specimen can be rescanned and compared with itself at several points in time (Dutilleul et al., 2005, 2008) and, we believe, represents an important future application of our technique.

Linear image filters, including the mean, median, and Gaussian blur filters, are used to effectively reduce image noise introduced by the imaging system (Seul et al., 2000). Image filters are often created for specific applications and modifications are typically required, as there are a large number of different image filters created to support image enhancement, compression, feature detection, and segmentation (Sahoo et al., 1988; Russ, 1992; Seul et al., 2000; Elliot and Heck, 2007b; Kawajiri et al., 2008). Currently there are no standards for differentiating tissues of herbaceous plants represented in X-ray μCT. A major limitation of the mean filter is that the treatment of all pixels equally meaning this filter will blur feature edges to the same degree that noise within the features is decreased. Although the median filter offers some improvement in the preservation of edges, it is less accurate in highly noisy images where the median pixel value is more likely to be that of noise. In comparison, a Gaussian blur preserves feature edges while reducing the amount of image noise by applying a weighted average of pixel values within the specified blur radius, the centre of the filter being the most weighted. The unequal weighting of pixel values makes the Gaussian blur more effective in especially noisy images over the median filter (Seul et al., 2000). Preliminary assessment of mean and median filters and comparison with a Gaussian blur image filter revealed that the latter is best suited for this study. In images of *E. vaginatum* corm, optimal blur radius ($\sigma$) was determined to be two pixels (Fig. 4).

### 3.5. Visualization of tissue structures: X-ray μCT vs. light microscopy

The ability to non-destructively acquire images and view them at any desired angle represents a tremendous advantage of X-ray μCT over destructive microscopy methods. In this manner an angle best suited to display and investigate complex tissues can be selected. Moreover, X-ray CT techniques represent a significant benefit in time saved for data acquisition. For a corm 5 mm to 1 cm in length, one would have to acquire between 500 and 1000 serial sections of embedded plant material and then digitize them to achieve a 3D image dataset at 10 μm thickness intervals, a virtually impossible task. Using our method, this represents between 80,000,000 and 160,000,000 voxels per corm image volume for a corm 4 mm in diameter. Using the in-house facilities at Guelph University, Canada, the 10 μm dataset used in this study represents approximately 3 h of scan time and 3 days of reconstruction. Comparatively, the 50 μm dataset was acquired and reconstructed in less than 1 day. The authors found that image interpretation was the time limiting factor in utilizing X-ray μCT.

The current study revealed several characteristics of sclereid clusters not identified in previous anatomical reports of Metcalfe (1971) and Cholewa and Griffith (2004). Sclereid clusters are lance shaped structures with an abaxial groove running their entire length (Fig. 5A, arrowhead) where vascular tissues are located. Every sclereid cluster was associated with a vascular bundle in this manner. These sclereid clusters were previously demonstrated to be highly lignified (Cholewa and Griffith, 2004), however, in X-ray μCT images sclereid clusters exhibited density differences between the periphery of the cluster and the interior (Fig. 5B, arrow). Upon closer examination with light microscopy, the reason for the density differences within sclereid clusters was identified. Sclereids comprising the periphery of the cluster had extremely thick secondary cell walls and very small lumena as compared to those in the interior which had relatively thin secondary cell walls and large lumena (Fig. 5C, arrow). The newly determined characteris-

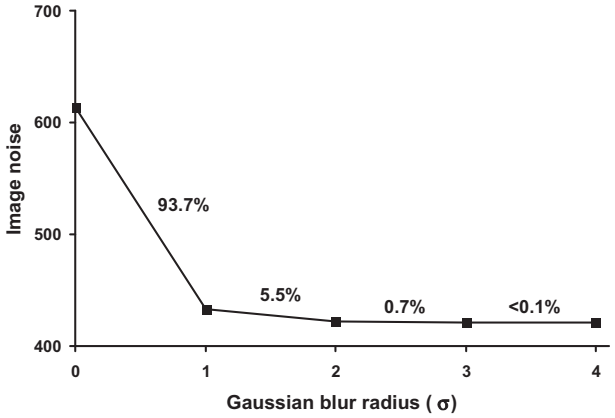


**Fig. 4.** Percent reductions in noise of Gaussian blur image series of Fig. 3. Image noise was calculated as the standard deviation of all voxels values (in HU) of each image in the blur series. A Gaussian blur radius ($\sigma$) of two pixels was chosen for use in this study as subsequent increases in blur amount resulted in <1% of noise reduced.

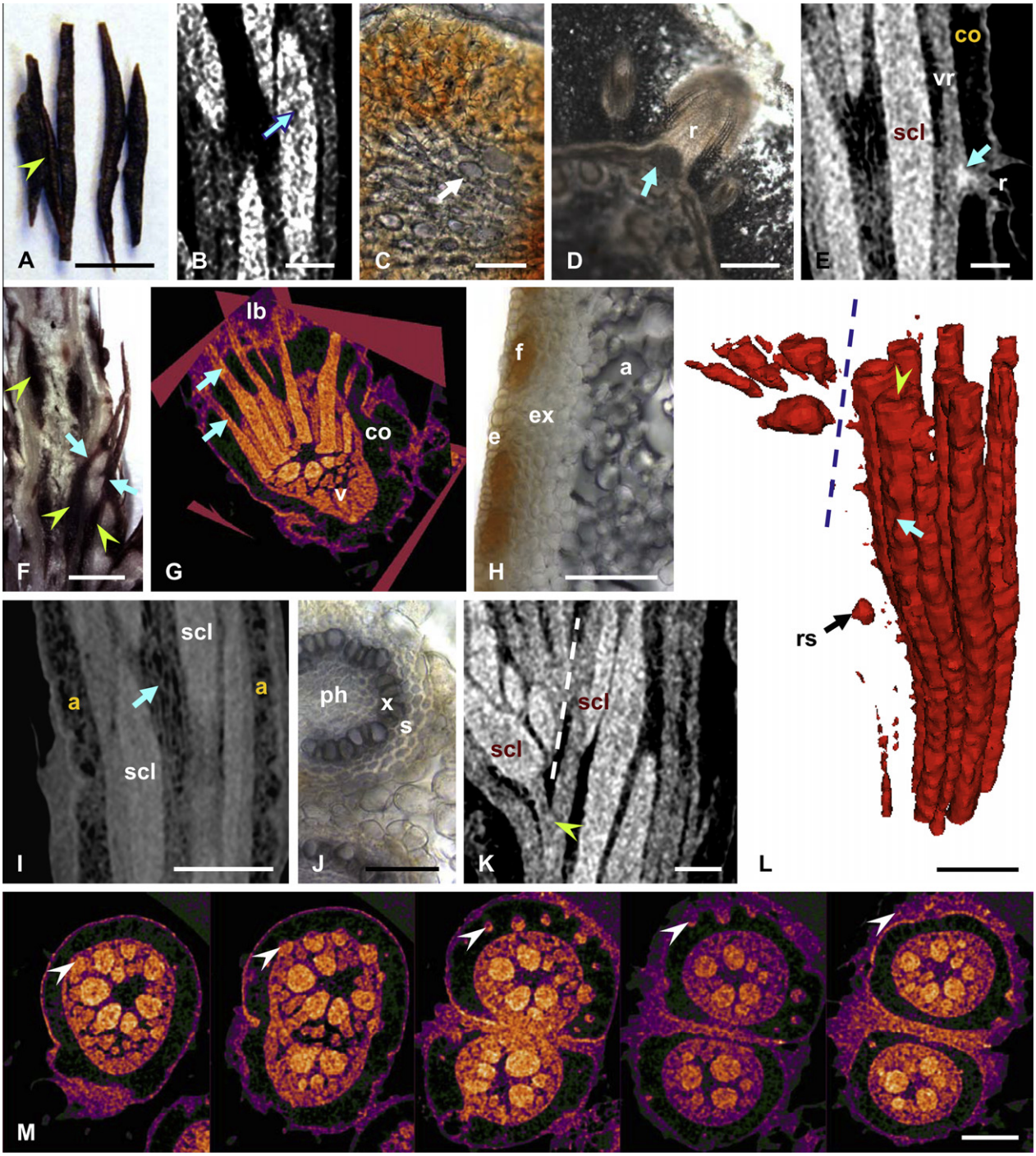


**Fig. 5.** (A–M) The morphology and anatomy of *E. vaginatum* corms visualized by X-ray μCT is confirmed by light microscopy. (A) Sclereid clusters dissected from the corm are lance shaped with abaxial groove (arrowhead) where vascular tissue was located. Bar = 2 mm. (B) X-ray μCT scanning evidently differentiates sclereids from surrounding corm tissues. Within sclereid clusters, differences in tissue density were observed where centre region was less dense (arrow). Image has been windowed to highlight sclereid clusters in long-section, l.s. Bar = 500 μm. (C) Light micrograph of thin secondary cell walls and large lumena (arrow) characteristic of sclereids in the centre of the cluster. Bar = 100 μm. (D) Light micrograph of root sclereid c.s. (arrow) in developing root (r). Bar = 500 μm. (E) Root sclereid (arrow) in root (r) visualized in X-ray μCT l.s. scl = sclereid cluster, vr = vascular ring, co = cortex. Image windowed for viewing of sclereid cluster and vascular tissues. Bar = 500 μm. (F) Longitudinally dissected corm exposing sclereid clusters (arrowheads) and their leaf traces (arrows). Bar = 2 mm. (G) X-ray μCT planar image cube showing sclereid clusters with leaf traces (arrows). Image has been falsely coloured based on voxel HU values, v = vascular tissues, co = cortex, lb = leaf bases. Image cube is $4 \times 5 \times 3.8$ mm. (H) Magnified light micrograph of epidermis, exodermis, and related fibre groups of the corm in c.s. These detailed structures were not distinguished by X-ray μCT technique, a = aerenchyma, e = epidermis, f = fibres, ex = exodermis. Bar = 100 μm. (I) X-ray μCT revealed vertical pattern of aerenchyma and sclereid clusters in the vascular cylinder (arrow). Image windowed to detail aerenchyma. Bar = 1 mm. (J) Detailed light micrograph of amphivasal vascular bundle. Phloem (ph) is surrounded by a ring of xylem (x). A lignified sheath (s) of cells surrounds the bundle. This amphivasal structure was not differentiated by X-ray μCT technique. Bar = 50 μm. (K) Vascular architecture of the corms can be determined with X-ray μCT. Arrowhead points to a vascular bundle branching. Soon after branching, vascular bundles are associated with developing sclereid clusters (scl). Sclereid cluster on left is in an outgrowing cormel, cluster on the right is in the parent corm. Line indicates corm-cormel interface. Image windowed for viewing of sclereid clusters and vascular tissues. Bar = 500 μm. (L) 3D map of sclereid clusters. Sclereids do not cross the corm-cormel interface, dashed line. Cormel is on the left, parent corm on the right. Root sclereids (rs) are also included in this map. Arrow points to sclereid cluster abaxial groove. Map is affected by density variations (arrowhead) of sclereid clusters viewed in (A) and (B). Bar = 1 mm. (M) Axial X-ray μCT image series showing cormel development in relation to parent corm. Left-most image is parent corm and the base of this division. Sclereid clusters (arrowheads) are formed within the vascular cylinder then diverge from the corm with leaf traces. Multiple sclereid clusters are associated with each leaf. Images falsely coloured as in (G). Image series encompasses 3 mm in the *Z*-direction. Bar = 1 mm.

tics of sclereid clusters are an attestation of the sensitivity and effectiveness of X-ray μCT for anatomical analysis of *E. vaginatum*. The proposed method allows for detection of these small anatomical features within intact corms and is therefore an excellent tool for assessing tissue structure of the *E. vaginatum* corm.

Cylindrically shaped objects are very resistant to physical plying forces and need only be reinforced on the outer edge to provide such structural strength, as in the shape of plant stems (Ennos, 1993). Therefore, the shape of sclereid clusters may provide structural support with minimal expense of resources acquired by *E. vaginatum* as this species is known to be highly efficient in nutrient acquisition and use in its native, nutrient poor habitats (Jonasson and Chapin, 1985; Chapin et al., 1979, 1993). The structure of sclereid clusters might thus reflect the high nutrient use efficiency of *E. vaginatum*.

Using light microscopy, sclereid masses, or root sclereids, were localized within developing adventitious roots at the point of their origin in the vascular ring (Fig. 5D, arrow). The root sclereids were also differentiated by X-ray μCT (Fig. 5E, arrow). Root sclereids were smaller than sclereid clusters associated with leaf traces. In addition, root sclereids did not exhibit differences in radiodensity or secondary cell wall thickness. These sclereid masses have been previously reported only in dead roots of *E. vaginatum* (Cholewa and Griffith, 2004). The presence of root sclereids in live roots may stabilize the root-corm connection when roots are subjected to changes in substrate conditions, such as swelling and substrate compaction due to water-level changes and freeze–thaw cycles. Strengthening of the root-corm connection could offer an advantage for *E. vaginatum* survival when growing in permafrost soils (Polozova, 1970; Wein, 1973; Chapin et al., 1979).

Sclereid clusters associated with leaf traces are formed within the vascular cylinder and then diverge from the corm into the bases of leaves (Fig. 5F). This relationship is impossible to view in long-section of fresh plant material because sclereid clusters easily tear away from the soft parenchyma and aerenchyma during sectioning. Cholewa and Griffith (2004) also reported the difficulty in sectioning of the corm due to the extreme density differences in sclereid clusters as compared to other more fragile aerenchyma and parenchyma tissues. These difficulties associated with light microscopy could be overcome with the advantages of the proposed X-ray μCT technique. The resultant dataset could be viewed at multiple angles simultaneously for analysis of tissue architecture and individual tissues could be falsely coloured depending on their HU values (Fig. 5G). False colouring improved visual interpretation of the images facilitating the distinction of sclereid clusters and leaf traces from other corm tissues.

A limitation of the proposed X-ray μCT technique is that differentiation of the protective outer layers of the corm was not possible. The *E. vaginatum* corm is protected from the environment by a single-layered epidermis and an underlying, multi-layered exodermis (Fig. 5H, e and ex, respectively) which irregularly contained fibres (Fig. 5H, f). Individual cells comprising these tissues are very comparable in dimensions and are extremely compact making their radiodensities too similar to be distinguished using our technique. Using a higher resolution scanning system, such as X-ray sub-micronCT or synchrotron radiation X-ray μCT, may also improve image quality and tissue differentiation. Syncrotron X-ray uCT has the added advantage that it utilizes a very high intensity, monochromatic X-ray beam, which eliminates noise associated with the polychromatic beam of X-ray tube-based CT scanners (Wildenschild et al., 2002; Salvo et al., 2003), such as the one used in this study. Synchrotron-based X-ray CT was recently applied to fresh plant material of bamboo, *Phyllostachys bambusoides* Sieb. et. Zucc., to assess water refilling of embolized vessel elements (Lee and Kim, 2008). However, synchrotron beam time is significantly more expensive and less accessible than X-ray tube-based CT scanners and, although the outer layers of the corm could not be differentiated in this study, our dataset still provides the physical relationship of this protective band in relation to other corm tissues. Moreover, the blurring of these layers does not limit interpretation of other corm tissue relationships.

*Eriophorum vaginatum* is adapted to water-logged wetland environments (Polozova, 1970; Wein, 1973; Chapin et al., 1979). Within these environments, plants must provide oxygen to submerged tissues by developing aerenchyma (Esau, 1960). Extensive aerenchyma tissue is located within the corm (Fig. 5H, a). This aerenchyma was easily visualized using X-ray μCT and the direction of large intercellular air spaces in aerenchyma was revealed to be parallel to sclereid clusters within the vascular cylinder (Fig. 5I, arrow and scl, respectively). This tissue arrangement allows for effective longitudinal gas exchange in providing oxygen to tissues located below water-level.

Vascular tissues formed a complex network within the corm. Individual vascular bundles were amphivasal with a ring of xylem surrounding the phloem (Fig. 5J). All bundles were sheathed by a weakly-lignified (weak positive staining with phloroglucinol-HCl, not shown) sheath of cells (Fig. 5J, s). Although this amphivasal tissue structure of the vascular bundles could not be differentiated by X-ray μCT, the overall architecture of vascular bundles could be followed (Fig. 5K, arrowhead).

*Eriophorum vaginatum* forms massive, complex tussocks by intravaginal tillering (Polozova, 1970; Chapin et al., 1979) whereby cormels develop inside leaf sheaths of the parent corm. Results show the vascular connections between the parent corm and cormel are in the form of vascular bundles diverging from the main corm into the developing cormel (Fig. 5K). It was discovered that soon after corm-cormel branching, vascular bundles were associated with developing sclereid clusters (Fig. 5K, scl) and became leaf traces. X-ray μCT was also successfully used by Maeda and Miyake (2009) to follow vascular tissue divergences in the inflorescence of Japonica type rice, *Oryza sativa*. The X-ray μCT technique could be applied to vascular structure research in other graminoid species.

Sclereid clusters do not cross the corm-cormel interface, but are initiated within each corm. This relationship can be easily demonstrated when an isosurface, or 3D map, of sclereids clusters is created (Fig. 5L). The sclereid cluster map was produced using the semi-automated segmentation technique within MicroView, which uses the Otsu (1979) algorithm. A small sub-volume containing between 15,000 and 20,000 voxels was selected in the main image volume. An image histogram for the sub-volume was automatically calculated and thresholded by MicroView. Although the sub-volume was selected to encompass two adjacent tissues in relatively similar amounts to refine the histogram, i.e. eliminate influence of other tissues on the histogram shape, the histogram used to calculate the threshold value was a bimodal distribution whereby two peaks were overlapping. Although the Otsu (1979) segmentation algorithm cannot easily distinguish overlapping peaks it, however, offers a simple, reasonably robust method to retain object shape (Sahoo et al., 1988). This suitability of the Otsu (1979) method to the present study is evident as the abaxial groove (Fig. 5L, arrow) was noticeable in the 3D map of sclereid clusters. Density differences observed in X-ray μCT images of sclereid clusters (Fig. 5L, arrowhead) and the presence of root sclereids were also apparent in this tissue map (Fig. 5L, rs).

X-ray μCT datasets provide excellent image series to follow tissue dynamics during corm development. The image series in Fig. 5M encompasses 3 mm in the longitudinal (*Z*) axis and shows cormel development in relation to parent corm and diverging leaf traces (arrowheads). Sclereid clusters formed within the vascular ring (Fig. 5M, arrowhead in left-most image), diverge into the cortex (middle image), and exit the corm with associated leaf traces (right image). Multiple sclereid clusters are associated with each

leaf. As *E. vaginatum* thrives in open wetland sites (Wein, 1973; Chapin et al., 1979), the structure of the corm must withstand potentially damaging wind forces on its leaves. Sclereid clusters are concluded to act as structural stabilizers to protect critical vasculature of the corm and leaf connection from mechanical damage.

Previous studies of plants by X-ray CT techniques have been largely limited to investigations whereby the magnitude of difference in radiodensity between the feature of interest and the background is relatively large, as in Steppe et al. (2004), DeVore et al. (2006), Hamza et al. (2007), and Kaminuma et al. (2008). However, a significant advantage of X-ray μCT scanners is that they can produce images with excellent low-contrast resolution, i.e. they can resolve soft tissues well, because they use lower energy X-ray spectra to form images (Ford et al., 2003). Our work demonstrates successful use of X-ray μCT for tissue analysis of fresh, hydrated corms of *E. vaginatum*, an herbaceous plant.

## 4. Conclusions

X-ray μCT is a promising new tool for botanical research. Herein a new X-ray μCT technique was developed and applied to the anatomical study of tissues within the corm of *E. vaginatum*. An isotropic voxel resolution of 10 μm was used to acquire X-ray μCT images and subsequent application of a Gaussian blur image filter with a blur radius ($\sigma$) of two pixels optimized corm imagery. Key aspects of *E. vaginatum* revealed by the proposed technique included the 3D architecture of sclereid clusters and the vascular network within the corm. Sclereid clusters associated with leaf traces diverge from the corm in groups into the base of each leaf. Interestingly, this divergence of sclereid clusters does not occur between vegetative generations but rather sclereid clusters develop within each new corm independently. This means that branching corms can easily be broken away from the primary tiller while the corm-leaf connection is structurally stabilized. Perhaps stabilizing the corm-leaf connection with sclereid clusters is ecologically significant for *E. vaginatum* survival within nutrient poor environments as physical damage to the vascular system of the corm-leaf connection may represent an ecologically considerable loss in nutrient acquisition potential. Conceivably, such protection of the link between the carbon assimilation (leaves) and carbon storage (corms) machinery of the *E. vaginatum* tussock would be of greater significance in the Arctic where the growing season is shorter than in the Boreal region. A lack in the stabilization of the branching connection between corms may not be as ecologically important for *E. vaginatum* survival as each corm is fully equipped to initiate growth on an individual basis. Moreover, the dense network of corms comprising the tussock may also stabilize neighbouring corms, thereby negating the requirement for extra stabilization via sclereid clusters. Corm tissue delineation within X-ray μCT images and small feature detection demonstrate that the proposed technique could be successfully used in future studies. The ability to study whole, live corms, in 3D and the identification of features not reported in previous light microscopy studies make it superior to destructive microscopy methods. As a future application, the proposed X-ray μCT technique could be used to detect alterations in tissue structure and chemistry of *E. vaginatum* corms in response to environmental change or be extended to the study of similar species.

## Acknowledgments

This project was supported by an NSERC IPS Scholarship to S.B., an NSERC Discovery grant to E.C., and an Ontario Research Fund grant co-held by P.K. Kaiser and P.G. Dunn of MIRARCO, Ontario, Canada, and G.S. A gracious thank you is extended to MIRARCO for their support as the industrial partner for the NSERC IPS Scholarship and for a MIRARCO Scholarship. We warmly thank Richard Heck, Department of Land Resource Science, University of Guelph, Guelph, Ontario, Canada, for access to his X-ray μCT scanner and to Tom Elliot for his technical assistance. Thank you to Grigori Sokolov who kindly translated the paper by Polozova from Russian to English. We also thank Kenneth Torrance and two anonymous reviewers for their helpful comments which improved our final manuscript.

## References

Archer, S., Tieszen, L.L., 1983. Effects of simulated grazing on foliage and root production and biomass allocation in an arctic tundra sedge (*Eriophorum vaginatum*). Oecologia 58, 92–102.

Chapin III, F.S., van Cleve, K., Chapin, M.C., 1979. Soil temperature and nutrient cycling in the tussock growth form of *Eriophorum vaginatum*. J. Ecol. 67 (1), 169–189.

Chapin III, F.S., Moilanen, L., Kielland, K., 1993. Preferential use of organic nitrogen for growth by a non-mycorrhizal arctic sedge. Nature 361, 150–153.

Cholewa, E., Griffith, M., 2004. The unusual vascular structure of the corm of *Eriophorum vaginatum*: implications for efficient retranslocation of nutrients. J. Exp. Bot. 55 (397), 731–741.

Cnudde, V., Masschaele, B., De Cock, H.E.V., Olstad, K., Vlaminck, L., Vlassenbroeck, J., Dierick, M., Witte, Y.D., Van Hoorebeke, L., Jacobs, P., 2008. Virtual histology by means *f* high-resolution X-ray CT. J. Microsc. 232, 476–485.

DeVore, M.L., Kenrick, P., Pigg, K.B., Ketcham, R.A., 2006. Utility of high resolution X-ray computed tomography (HRXCT) for paleobotanical studies: an example using London Clay fruits and seeds. Am. J. Bot. 93 (12), 1848–1851.

Duffy, L.K., Kaiser, C., Ackley, C., Richter, K.S., 2001. Mercury in hair of large Alaskan herbivores: routes of exposure. Alces 37, 293–301.

Dutilleul, P., Lontoc-Roy, M., Prasher, S.O., 2005. Branching out with a CT scanner. Trends Plant Sci. 10 (9), 411–412.

Dutilleul, P., Han, L., Smith, D.L., 2008. Plant light interception can be explained via computed tomography scanning: Demonstration with pyramidal cedar (*Thuja occidentalis*, Fastigiata). Ann. Bot. 101, 19–23.

Elliot, T.R., Heck, R.J., 2007a. A comparison of 2D vs. 3D thresholding of X-ray CT imagery. Can. J. Soil Sci. 87, 405–412.

Elliot, T.R., Heck, R.J., 2007b. A comparison of optical and X-ray CT technique for void analysis in soil thin section. Geoderma 141, 60–70.

Ennos, A.R., 1993. The mechanics of the flower stem of the sedge *Carex acutiformis*. Ann. Bot. 72, 123–127.

Esau, K., 1960. Anatomy of Seed Plants, second ed. John Wiley and Sons, New York, USA.

Evans, N.J., McInnes, B.I.A., Squelch, A.P., Austin, P.J., McDonald, B.J., Wu, Q., 2008. Application of X-ray micro-computed tomography in (U–Th)/He thermochronology. Chem. Geol. 257, 101–113.

Farr, R.F., Allisy-Robers, P.J., 1998. Physics for Medical Imaging. Harcourt Brace and Company Ltd., London. p. 276.

Ford, N.L., Thornton, M.M., Holdsworth, D.W., 2003. Fundamental image quality limits for microcomputed tomography in small animals. Med. Phys. 30 (11), 2869–2877.

Fromm, J.H., Sautter, I., Matthies, D., Kremer, J., Schumacher, P., Ganter, C., 2001. Xylem water content and wood density in spruce and oak trees detected by high-resolution computed tomography. Plant Physiol. 127, 416–425.

Hamza, M.A., Anderson, S.H., Aylmore, L.A.G., 2007. Computed tomographic evaluation of osmotica on shrinkage and recovery of lupin (*Lupinus angustifolius* L.) and radish (*Raphanus sativus* L.) roots. Environ. Exp. Bot. 59, 334–339.

Hounsfield, G.N., 1973. Computerized transverse axial scanning (tomography): part 1. Description of system. Br. J. Radiol. 46, 1016–1022.

Huopalainen, M., Tuittila, E.-S., Vanha-Majamaa, I., Nousiainen, H., Laine, J., Vasander, H., 2000. The potential of soil seed banks for revegetation of bogs in SW Finland after long-term aerial pollution. Ann. Bot. Fenn. 37, 1–9.

Jassogne, L., McNeill, A., Chittleborough, D., 2007. 3D-visulalization and analysis of macro- and meso-porosity of the upper horizons of a sodic, texture-contrast soil. Eur. J. Soil Sci. 58, 589–598.

Jonasson, S., Chapin III, F.S., 1985. Significance of sequential leaf development for nutrient balance of the cotton sedge, *Eriophorum vaginatum* L. Oecologia 67, 511–518.

Jones, D.R., Eason, W.R., Dighton, J., 1998. The fate of $^{137}$Cs in senescing roots of *Eriophorum vaginatum* L. J. Environ. Radioact. 40, 271–288.

Kalender, W.A., 2005. Computed Tomography Fundamentals, System Technology, Image Quality, Applications, second revised ed. Publicis Corporate Publishing, Erlangen, Germany.

Kaminuma, E., Yoshizumi, T., Wada, T., Matsui, M., Toyoda, T., 2008. Quantitative analysis of heterogeneous spatial distribution of *Arabidopsis* leaf trichomes using micro X-ray computed tomography. Plant J. 56, 470–482.

Kawajiri, S., Zhou, X., Zhang, X., Hara, T., Fujita, H., Yokoyama, R., Kondo, H., Kanematsu, M., Hoshi, H., 2008. Automated segmentation of hepatic vessels in non-contrast X-ray CT images. Radiol. Phys. Technol. 1, 214–222.

Ketcham, R.A., Carlson, W.D., 2001. Acquisition, optimisation and interpretation of X-ray computed tomographic imagery: applications to the geosciences. Comput. Geosci. 27, 381–400.

Lavoie, C., Grosvernier, P., Girard, M., Marcoux, K., 2003. Spontaneous regevetation of mined peatlands: an useful restoration tool? Wetl. Ecol. Manage. 11, 97–107.

Lee, S.-J., Kim, Y., 2008. *In vivo* visualization of the water-refilling process in xylem vessels using X-ray micro-imaging. Ann. Bot. 101, 595–602.

Leroux, O., Leroux, F., Bellefroid, E., Claeys, M., Couvreur, M., Borgonie, G., Van Hoorebecke, L., Masschaele, B., Viane, R., 2009. A new preparation method to study fresh plant structures with X-ray computed tomography. J. Microsc. 233, 1–4.

Lontoc-Roy, M., Dutilleul, P., Prasher, S.O., Han, L., Brouillet, T., Smith, D.L., 2006. Advances in the acquisition and analysis of CT scan data to isolate a crop root system from the soil medium and quantify root system complexity in 3-D space. Geoderma 137, 231–241.

Maeda, E., Miyake, H., 2009. A non-destructive tracing with an X-ray micro CT scanner of vascular bundles in the ear axes at the base of the lower level rachis-branches in Japonica type rice (*Oryza sativa*). Jpn. J. Crop Sci. 78 (3), 382–386.

Markert, B., Thornton, I., 1990. Multi-element analysis of an English peat bog soil. Water Air Soil Pollut. 49, 113–123.

Marziliano, P., Dufaux, F., Winkler, S., Ebrahimi, T., 2004. Perceptual blur and ringing metrics: application to JPEG2000. Signal Process. Image Commun. 19, 163–172.

Metcalfe, C.R., 1971. Anatomy of the Monocotyledons. *V. Cyperaceae*. Caledon Press, Oxford. pp. 260–261.

Otsu, N., 1979. A threshold selection method from gray-level histograms. IEEE Trans. Sys. Man Cybern. 9 (1), 62–66.

Pierret, A., Moran, C.J., Doussan, C., 2005. Conventional detection methodology is limiting our ability to understand the roles and functions of fine roots. New Phytol. 166, 967–980.

Polozova, T.G., 1970. Biological features of *Eriophorum vaginatum* L. as a tussock former (based on observations in tundras of western Taimyr). Bot. Zh. 55, 431–442.

Racine, C.H., 1994. Long-term recovery of vegetation on 2 experimental crude-oil spills in interior Alaska black spruce taiga. Can. J. Bot. 72, 1171–1177.

Racine, C.H., Johnson, L.A., Viereck, L.A., 1987. Patterns of vegetation recovery after tundra fires in northwestern Alaska. Arct. Alp. Res. 19, 461–469.

Russ, J.C., 1992. The Image Processing Handbook. CRC Press Inc.

Sahoo, P.K., Soltani, S., Wong, A.K.C., 1988. A survey of thresholding techniques. Comput. Vis. Graph. Image Process. 41, 233–260.

Salvo, L., Cloetens, P., Maire, E., Zabler, S., Blandin, J.J., Buffière, J.Y., Ludwig, W., Boller, E., Bellet, D., Josserond, C., 2003. X-ray micro-tomography an attractive characterisation technique in materials science. Nucl. Instrum. Methods Phys. Res. B 200, 273–286.

Seul, M., O'Gorman, L., Sammon, M.J., 2000. Practical Algorithms for Image Analysis. Description, Examples, and Code. Cambridge University Press, Cambridge, UK.

Steppe, K., Cnudde, V., Girard, C., Lemeur, R., Cnudde, J.-P., Jacobs, P., 2004. Use of X-ray computed microtomography for non-invasive determination of wood anatomical characteristics. J. Struct. Biol. 148, 11–21.

Stevens, C., 2006. Primary revegetation on processed kimberlite at De Beers's Victor Diamond Project near Attawapiskat, Ontario. M.Sc. Thesis, Department of Biology, Laurentian University, Canada.

Stock, S.R., Nagaraja, S., Barss, J., Dahl, T., Veis, A., 2003. X-ray microCT study of pyramids of the sea urchin *Lytechinus variegatus*. J. Struct. Biol. 141, 9–21.

Stuppy, W.H., Maisano, J.A., Colbert, M.W., Rudall, P.J., Rowe, T.B., 2003. Three-dimensional analysis of plant structure using high-resolution X-ray computed tomography. Trends Plant Sci. 8 (1), 2–6.

Sutton, M.D., 2008. Tomographic techniques for the study of exceptionally preserved fossils. Proc. R. Soc. B 275, 157–1593.

Tondi, G., Blacher, S., Léonard, A., Pizzi, A., Fierro, V., Leban, J.M., Celzard, A., 2009. X-ray microtomography studies of tannin-derived organic and carbon foams. Microsc. Microanal. 15, 384–394.

Torrance, J.K., Elliot, T., Martin, R., Heck, R.J., 2008. X-ray computed tomography of frozen soil. Cold Reg. Sci. Technol. 53, 75–82.

Van den Bulcke, J., Boone, M., Van Acker, J., Van Hoorebeke, L., 2009a. Three-dimensional X-ray imaging and analysis of fungi on and in wood. Microsc. Microanal. 15, 395–402.

Van den Bulcke, J., Boone, M., Van Acker, J., Stevens, M., Van Hoorebeke, L., 2009b. X-ray tomography as a tool for detailed anatomical analysis. Ann. Forensic Sci. 66, 508.

Wang, Y., 2007. Morphological characterization of wood plastic composite (WPC) with advanced imaging tools: developing methodologies for reliable phase and internal damage characterization. M.Sc. Thesis, Department of Wood Science and Engineering, Oregon State University, USA.

Wein, R.W., 1973. *Eriophorum vaginatum* L. J. Ecol. 61 (2), 601–615.

Wildenschild, D., Hopmans, J.W., Vaz, C.M.P., Rivers, M.L., Rickard, D., Christensen, B.S.B., 2002. Using X-ray computed tomography in hydrology: systems, resolutions, and limitations. J. Hydrol. 267, 285–297.

Yang, J., Liu, L., Jiang, T., Fan, Y., 2003. A modified Gabor filter design method for fingerprint image enhancement. Pattern Recognit. Lett. 24, 1805–1817.